ASIA-PACIFIC SOLAR RESEARCH CONFERENCE
2016
Peer Reviewed
2016 Solar Research Conference

Mark Baldry

Preliminary Characterisation of a Rooftop Solar Furnace

M. Baldry[1] and R.A. Taylor[1]
[1] *School of Mechanical and Manufacturing Engineering, The University of New South Wales (UNSW), Kensington, New South Wales 2052, Australia*
E-mail: mark.baldry@unsw.edu.au

Abstract

The aim of this paper is to characterise the performance of the recently installed rooftop solar furnace at the University of New South Wales. The total power output, focal spot geometry, and peak flux ratio are determined using calorimetric and radiometric methods. A spiral-wound, monotube receiver was used to calculate the system's peak power output (ϕ_p) on a clear day at solar noon, using water as the heat transfer fluid. The ϕ_p based on this experiment is approximately 6.4±1.3 kW. The system's peak flux concentration was determined using reflection mode radiometry with a consumer grade DSLR camera. The focal spot adopted an elliptical geometry, with a peak flux that exceeded 1±0.03 MW/m^2, compared to the design estimate of 0.85 MW/m^2.

1. Introduction

Solar reactor technology has been investigated for over three decades and shows promising potential applications such as the synthesis of sustainable solar fuels (Ingel, Levy et al. 1992). A novel reactor design was recently developed that aims to exploit photothermal catalysts to achieve solar chemical processing at lower temperatures compared to conventional thermal systems. The majority of solar furnace systems around the world vary in their design, though the basic components typically include a (1) tracking heliostat, (2) concentrator, (3) cavity receiver, and (4) shutters to attenuate the irradiance on the concentrator (Lewandowski, Bingham et al. 1991, Neumann and Groer 1996, Lee, Chai et al. 2014). The key details of various furnaces are summarised in Table 1. Each of these systems is unique, with variations in dish and heliostat design. Two key characterisation metrics for any solar furnace are the peak power output (ϕ_p), and the peak flux ratio (C_p); these are essential to track performance, as well as for receiver design. The UNSW Solar Furnace Laboratory (SFL) was designed to deliver 7 kW of power and an 850 peak flux ratio at ideal conditions (Taylor, Yang et al. 2014). It has recently been commissioned and requires thorough characterisation before proceeding with reactor testing.

Radiometry is used to map of the radiation flux distribution across a solar furnace's focal spot (Sarwar, Georgakis et al. 2014). This non-invasive technique only requires a CCD or CMOS camera, Lambertian target, neutral density filters, and a calibrated sensor (Ulmer, Reinalter et al. 2002, Ho and Khalsa 2012, Lee, Chai et al. 2014). The process essentially involves taking a greyscale image of an illuminated receiver plate, placed perpendicular to the optical axis at the focal spot (Johnston 1998, Parretta, Privato et al. 2006). Image rectification adjusts for perspective distortion whilst flux may be calculated from raw pixel data using a conversion factor (F_c) (Sarwar, Georgakis et al. 2014). Peak power output, on the other hand, may be estimated using simple calorimetric methods, such as measuring the temperature increase of a heat transfer fluid across a solar receiver to determine sensible heat change. The approach adopted in this work is detailed in section 3.1.

Table 1: Major solar furnace research facilities around the world

Peak Output [kW]	Peak Flux Ratio [Suns]	Primary Concentrator Aperture Area [m^2]	Location	Reference
70	-	100	Tohoku University	Sakurai, Kamada et al. (1964)
17	4000	5.7	Paul Scherrer Institute (PSI)	Ries and Schubnell (1990); Schubnell, Keller et al. (1991)
-	-	0.28	University of Technology, Malaysia	Chen, Chong et al. (2002)
-	-	0.4	University of Science and Technology of China	Chong, Lim et al. (2011); Lim and Li (2009)
30	-	36	Mexico	Riveros-Rosas, Herrera-Vasquez et al. (2010); Perez-Enciso, Riveros-Rosas et al. (2014)
1000	-	2160	CNRS Solar Energy Laboratory	Trombe and Vinh (1973); Sammouda, Royere et al. (1999)
-	25000	11.5	National Renewable Energy Laboratory (USA)	Lewandowski, Bingham et al. (1991)
20	4000	39	German Aerospace Centre (DLR)	Neumann and Groer (1996); Rohner and Neumann (
40	5050	62	Korean Institute of Energy Research	Lee, Chai et al. (2014)
60	2847	98.5	Plataforma Solar de Aleria, Spain (PSA)	Roldan, Zarza et al. (2015); Roldan and Monterreal (2014)
5	6000	8.77	Plataforma Solar de Aleria, Spain (PSA)	Rodriguez, Canadas et al. (2014)
7	7000	-	University of Minnesota	Diver, Carlson et al. (1983)
15	10000	41.9	Weizmann Institute of Science	Levy, Rosin et al. (1989)
1000	-	-	Uzbekistan Academy of Sciences	Abdurakhmanov, Akbarov et al. (2008); Abdurakhmanov, Akbarov et al. (2008)
6.3	>1000	11.9	University of New South Wales	Current work

2. SFL Solar Furnace

The detailed specifications of the SLF rooftop solar furnace are available in Taylor, Yang et al. (2014) and will only be briefly outlined here. It consists of a 14 m^2 2-axis tracking heliostat (Figure 1), and a stationary concentrating dish (Figure 2) with a 12 m^2 aperture. Both the heliostat and dish fold down to minimise wind loading for increased safety. The coiled tube receiver used for calorimetric testing is shown in Figure 3. The heliostat and concentrator are composed of three panels, each covered with eighteen 12x12", 0.95 mm silvered glass mirror tiles that match the panel curvature. Compared to many of the furnaces in Table 1, this is a compact and low complexity system, with a total length of 10.7 m and a concentrator focal length of 4.88 m. Its inherent simplicity mitigates the need for extensive control systems and large areas, making it suitable for rooftop spaces. Prior to testing, the heliostat and concentrator mirror panels had to be aligned. Each panel is fitted with three adjustable anchor screws to tune its orientation relative to the support frame. Alignment was guided by manually optimising the geometry and location of the focal spot, as viewed with highly attenuating welding masks.

Figure 1: SFL solar furnace heliostat

Figure 2: SFL concentrator

Figure 3: Coiled tube receiver

3. Methods

3.1 Calorimetric Analysis

The total, instantaneous power output of the furnace was determined using a custom-built receiver, consisting of a spiral-wound, stainless-steel tube housed in an insulated cavity (Figure 3). The tube is coiled into a conical frustum shape, facilitating an even distribution of light across its entire length, and features a conical, Zircar 'plug' that that reflects incident light back on the tube. Thermocouples have been fitted to the inlet and outlet of the receiver to provide instantaneous measurements of temperature. A simple energy balance around the system (Eq. 1) is used to calculate the total power delivered by the solar furnace (ϕ_{SF}), where $\Delta\dot{H}_w$ is the sensible heat change of the flowing water as it passes through the receiver.

$$\alpha_R^{sw}\phi_{SF} = \Delta\dot{H}_w + \dot{Q}_{cv}^{l} + \dot{Q}_{rd}^{l} + \dot{Q}_{cd}^{l} \quad (1)$$

It is assumed that heat losses from conduction ($\dot{Q}_{cd}^{l}$) to the receiver housing are negligible, due to insulation. The flowrate of water through the receiver ($\dot{m}_w$) will be set such that the tubes are kept relatively cool, thereby making the thermal loss from radiation ($\dot{Q}_{rd}^{l}$) as well as the convective heat losses ($\dot{Q}_{cv}^{l}$) relatively small. To justify these assumptions, some preliminary loss calculations have been made. The $\dot{Q}_{rd}^{l}$ accounts for around 15 W at the outlet temperature of 40 °C, based on the Stefan-Boltzmann law. Convective losses are more difficult to calculate for

cavity receivers, due to complex internal geometries and forced convection effects, leading many authors to rely on numerical modelling or experimental methods (Clausing 1981, Ma 1993, Abbasi-Shavazi, Hughes et al. 2015). Furthermore, empirical models for cavity convection may not retain their validity for different designs (Taumoefolau, Paitoonsurikarn et al. 2004). We selected the method proposed by Leibfried and Ortjohann (1995), which was developed for hemispherical receivers with upward facing tilt angles, and found to have good agreement with experimental data by Taumoefolau, Paitoonsurikarn et al. (2004). This resulted in an estimated convective loss of 12 W, but only accounts for natural convection. For comparison, a vertical flat plate under forced convection with an identical heat transfer area, using the correlation of Serth and Lestina (2014), experiences a loss of approximately 45 W for a nominal wind speed of 25 m/s parallel to the plate. Ma (1993) argues that flat plate correlations do not accurately represent cavity convective losses for wind speeds less than about 4 m/s, highlighting the need for a cavity-specific model. Since the order of magnitude in both of these correlations is much less than the expected power (~7 kW), convective losses are considered negligible, with further analysis of the cavity's thermal behaviour left for future work. The energy balance now simplifies to Eq. (2), where the only unknown quantities are ϕ_{SF} and the solar weighted absorptivity of the tubes (α_R^{sw}).

$$\alpha_R^{sw}\phi_{SF} = -\dot{m}_w Cp_w(T_w^{out} - T_w^{in}) \quad (2)$$

The coiled tube shows clear signs of surface oxidation, so to avoid the need to optically characterise the complex internal surface of the receiver, the tubes were pained with a high temperature, matte black Dupli-Color High Heat aerosol paint. The α_R^{sw} of this paint was measured to be 0.94±0.009 over the wavelength range 0.28 μm to 20 μm, using the AM1.5 solar spectrum.

3.2 Equipment and Estimated Uncertainty

A consumer Nikon d5100 CMOS camera with 14-bit depth was used with an 18-70 mm Nikon zoom lens. The 14-bit depth sensor records up to 16385 tones per RGB channel, giving an approximate resolution uncertainty of ±0.006%. An exposure time of 250 μs was used with various aperture settings for flux mapping. A square, 300 mm Zircar plate was selected as the target, due to its high temperature resistance and diffuse reflectance behaviour (measured solar-weighted diffuse reflectance of 0.87±0.009). A series of Formatt-Hitch neutral density filters with optical density of 0.6, 1.5 and 3 were used to mitigate sensor saturation. Temperature data was collected with two K-type thermocouples (Class 2) and a YC-747U data logger, and flow rate was determined gravimetrically. Thermocouple standard error margin of ±2.5°C was used whilst the error in flow rate measurement was conservatively estimated at ±5%. Absorptivity and reflectivity were measured using a Perkin Elmer 150 mm optical integrating sphere, with an estimated uncertainty of ±1%. DNI data was collected with an EKO pyrheliometer MS-56, whilst global irradiance on an inclined target was collected using a Middleton Solar EQ08 First Class pyranometer. These devices have a reported uncertainty of ±1% and ±3%, respectively.

3.3 Camera Calibration and Image Rectification

Camera positioning relative to the target impacts the extent of image rectification required, yet is constrained by the design of the solar furnace. In most cases, the camera must be positioned off-axis, leading to perspective distortions that must be corrected (Ulmer, Reinalter et al. 2002, Mojiri, Stanley et al. 2015). In this work, the camera was positioned slightly off axis, directly under the concentrator, resulting in minimal perspective distortion. Rectification was carried out using a method based on that developed by Parretta, Privato et al. (2006) and Mojiri, Stanley et al. (2015), which uses the open-source camera calibration toolbox by Bouguet (2015). Sixteen images were taken of a calibration checkerboard (196 squares with 28 mm sides) at various

orientations, whilst keeping the camera location, orientation, and settings constant. Intrinsic parameters are estimated with the toolbox and used to correct the images for distortion arising from the camera's hardware, such as lens aberration. The extrinsic parameters instead describe the position of the planar target relative to the camera, and are used to rectify perspective distortion. To compute the extrinsic parameters of a particular camera-target system, which will be used in the flux mapping algorithm, an image is taken of the checkboard in the exact, coplanar location of the target plate and then processed with the toolbox (Mojiri, Stanley et al. 2015).

3.4 Conversion factor (F_c)

As mentioned earlier, a conversion factor is required to convert the raw image data into irradiance units. A common method for finding F_c involves incorporating a heat flux gauge into the reflector target at the point of maximum flux, and comparing the measured value with the raw image. (Neumann and Groer 1996, Johnston 1998, Haueter, Seitz et al. 1999, Lee, Chai et al. 2014 , Sarwar, Georgakis et al. 2014). Ulmer, Reinalter et al. (2002) argue that a steep temperature gradient across the sensor in this process may lead to significant uncertainty, and instead compare the total power of the furnace with the sum of the pixel values (px) in a raw flux image. However, this method requires accurate prior knowledge of the target's optical properties, and the furnace's total power output, which varies due to meteorological conditions and equipment wear. An alternative method involves taking an image of an object with a known radiance profile for use as the reference standard. Ho and Khalsa (2012) calculated F_c by taking images of the sun and comparing the pixel readings against on-site DNI measurements. A similar approach is taken in this work. The Lambertian target is mounted adjacent and coplanar to a pyranometer. During a clear day, the target is photographed, and the mean pixel intensity across the surface is extracted from the image. This is compared to the measured global irradiance to calculate the conversion factor F_c. Whilst this averaged approach neglects variation in pixel response across the sensor and surface heterogeneity across the target, it is simple to set up and control. The conversion factor may also be scaled to account for the use of different neutral density filters.

3.5 Sources of Uncertainty

Uncertainty and error in the characterisation process may arise from multiple sources, including (1) the camera's optics, (2) receiver heat losses, (3) optical inefficiency of the mirrors, and (4) transient weather effects. The CMOS sensor digitises the relative intensity of incoming light by converting it into a voltage (Ho and Khalsa 2012). Once converted into a greyscale image, the light intensity of the subject is represented by a pixel 'greyvalue' (*gv*). Several authors have highlighted that consumer grade camera sensors may not exhibit a linear relationship between input power and pixel value (Ulmer, Reinalter et al. 2002, Lee, Chai et al. 2014, Sarwar, Georgakis et al. 2014). This may misrepresent the relative brightness within an image, rendering comparison difficult. The intensity response curve for the Nikon d5100 is shown in Figure 4. Successive images of a uniformly illuminated target were taken with different exposure times. The mean pixel intensity across the surface of the plate was calculated using the flux mapping method outlined above. This is similar to the method outlined by Mojiri, Stanley et al. (2015), as well as that of Ho and Khalsa (2012), who instead varied aperture size. These results suggest that areas of the flux map that lie within the non-linear region should be interpreted with caution, and compared against images with more strongly attenuating filters. It is important to remember also that the sensor has a lower limit on resolution. Comparison of multiple images spanning the brightness range is therefore required to understand the full extent of the focal spot.

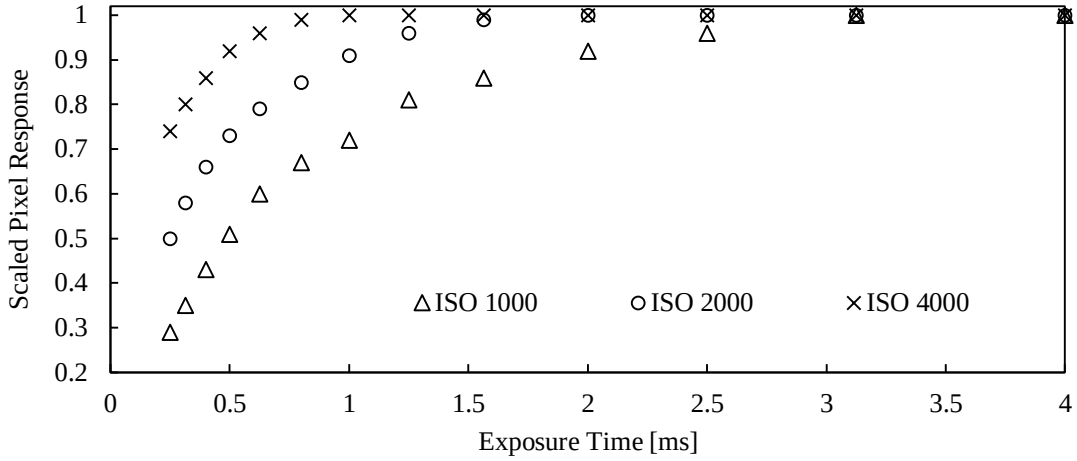

Figure 4: Sensor intensity response curve for the Nikon d5100

A key shortcoming of this radiometric method is that each CMOS sensor has a specific spectral response profile. Prasad, guyen et al. (2013) performed experimental and simulated spectral response analyses of various CMOS cameras, including the Nikon d5100. They show significant variation in the intensity peaks corresponding to each RGB colour channel, as well as drops in intensity for intermediate wavebands. Additionally, there is limited sensitivity for wavelengths >680 nm, corresponding to the red portion of the spectrum. The development of a model to account for this spectral response profile of the camera's sensor is left for future work.

4. Results & Discussion

The calorimetric test was conducted between 11:30 am and 11:40 am on 03/11/2016 under clear sky conditions, coinciding with solar noon (11:38 AM). An on-site weather station measured the mean direct normal irradiance during this period to be 910.8±9.1 W/m^2 and mean ambient temperature of 23.3±2.5°C. Wind speed varied from 0 to 25 m/s during the testing period, which may impact the convective heat losses from the coiled tube receiver. Over the 10-minute test period, the water flow rate was measured six times with a mean of 0.054±0.0027 kg/s. Water inlet and outlet temperature during the test period were approximately 22.6±2.5°C and 40.4±2.5°C, respectively. The mean power output of the solar furnace was then calculated using the average temperature, in conjunction with Eq. (2). At the time of testing, only two of the three concentrating mirror panels were operational, giving a measured power output of 4.3±0.9 kW. When scaled to three mirrors, this gives an estimated maximum power (ϕ_{SF}) of 6.4±1.3 kW, compared to the design estimate of 7 kW. Future work will aim to reduce the uncertainty of this measurement, mitigate heat loss, and arrive at a more robust estimate of peak power output.

The flux map series in Figure 5 shows the results of the radiometric methods outlined above and is presented in raw intensity. Each image was taken with a different combination of filters, resulting in the optical density indicated. The sun tracking system was not operational so manual tracking was used, resulting in a slight change in the position of the focal spot between images. The 13 cm receiver aperture has been overlain as a dotted circle on each flux image to qualitatively assess radiation spillage. It is apparent that the majority of the concentrated light falls within this region, with only limited spillage of low intensity light, as seen in image (A) and (B). Further analysis is required to quantify the magnitude of this loss whilst more stringent optical alignment may lead to a tighter focal spot with less spillage.

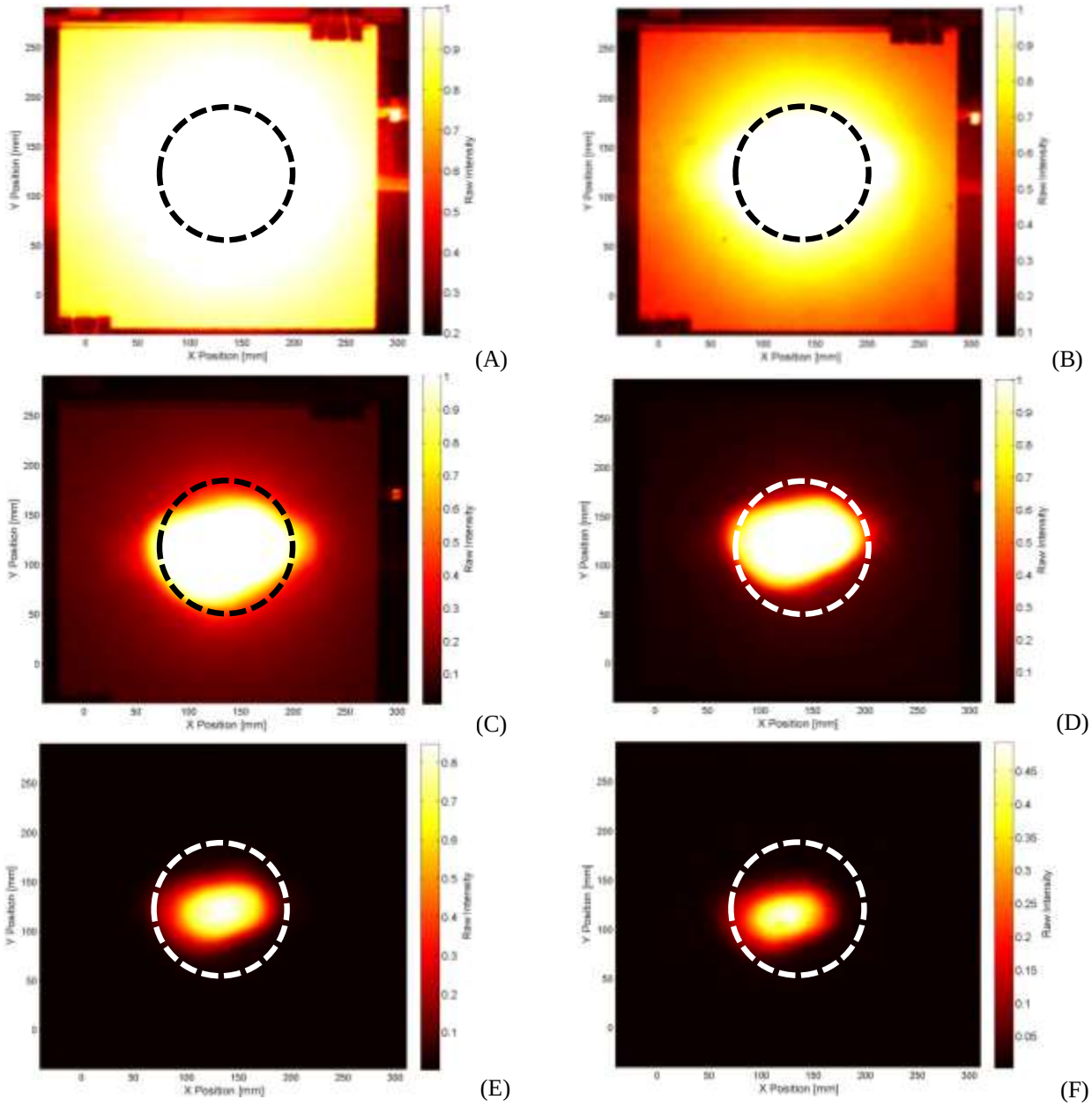

Figure 5: Flux map series using Nikon d5100 with ISO4000 sensitivity, 0.25 ms shutter speed and f29 aperture, taken at 1:45 pm on 17/11/2016. Filter optical density for each image is as follows: (A) 0, (B) 0.6, (C) 1.5, (D) 2.1, (E) 3, (F) 3.6. Dotted circle represents 13 cm receiver aperture and flux is shown in relative intensity units.

Given the steep gradient across the flux map, no single image was able to resolve both the high and low intensity regions of the focal spot. The maximum flux was estimated to be >1 MW/m^2 using image (F), as the maximum intensity value was comfortably below the nonlinear threshold for the ISO4000 image series. A conversion factor (F_c) was calculated for each flux image, corresponding to the specific set of experimental parameters. The F_c used to estimate the peak flux was 2285±68.5 kW/m^2/*gv*, with a mean calibration intensity of 0.05206±0.000003, irradiance of 939.7±28.2 W/m^2, and accounts for the optical density of the filters used. This resulted in an uncertainty in the peak flux of approximately ±3%. The elliptical portion of the focal spot that reached this intensity was only 17 mm by 12 mm, covering an area of ~160 mm^2 and capturing around 160 W. A composite data set was constructed by crudely overlaying the

data from images (B) through (F), selecting only those regions that were within the sensor's acceptable response region. The total incident power was estimated at 4.3±0.13 kW (~66% of the measured peak power output) by numerically integrating this data set and accounting for the reflectivity of the Zircar plate. It should be stressed that this is only a preliminary calculation of the power input using the flux data and requires significant further refinement. Potential sources of error include the spectral response of the sensor mentioned in section 3.5, omission of long wavelength emission from the hot plate, and weather conditions (the two tests were conducted on different days and at different times). Notwithstanding this, it is encouraging to see that the calculated total power is in the same order of magnitude as the experimental measurement. It should also be noted that the ceramic plate was not cooled during testing, leading to fracturing from thermal stresses across the spot.

5. Conclusions & Future Work

The UNSW solar furnace has been characterised using simple calorimetric and radiometric methods and found to have a peak flux in excess of 1±0.03 MW/m^2 and an estimated peak power output of 6.4±1.3 kW. The results will inform the future design of high temperature solar receivers for use in this rig. Future work will involve a full power calorimetric test, improved optical alignment of the system, and an investigation of the focal spot geometry at varying distances from the convergence point.

6. References

Abbasi-Shavazi, E., G. O. Hughes and J. D. Pye (2015). Investigation of heat loss from a solar cavity receiver. International conference on concentrating solar power and chemical engergy systems, SolarPACES 2014, Energy Procedia.

Abdurakhmanov, A., P. Akbarov, Z. Akhadov, M. Mamatkosimov, Y. Sobirov and U. Turaeva (2008). "Creating melting furnaces based on the large solar furnace." Applied Solar Energy **44**(4): 284-287.

Abdurakhmanov, A., P. Akbarov and Y. Sobirov (2008). "Analysis of operating characteristics of various smelting furnaces on a large solar furnace." Applied Solar Energy **44**(1): 24-27.

Bouguet, J. (2015). "Camera Calibration Toolbox for Matlab." from http://www.vision.caltech.edu/bouguetj/calib_doc/.

Chen, Y., K. Chong, C. Lim, B. Lim, K. Tan, O. Aliman, T. Bligh, B. Tan and G. SIsmail (2002). "Report of the first prototype of non-imaging focusing heliostat and its application in high temperature solar furnace." Solar Energy **72**(6): 531-544.

Chong, K., C. Lim and C. Hiew (2011). "Cost-effective solar furnace system using fixed geometry non-imaging focusing heliostat and secondary parabolic concentrator." Renewable Energy **36**: 1595-1602.

Clausing, A. M. (1981). "An analysis of convective losses from cavity solar central receivers." Solar Energy **27**(4): 295-300.

Diver, R., D. Carlson, F. Macdonald and E. Fletcher (1983). "A new high-temperature solar research furnace." Transactions of the ASME **105**: 288-293.

Haueter, P., T. Seitz and A. Steinfeld (1999). "A new high-flux solar furnace for high-temperature thermochemical research." Journal of Solar Energy Engineering **121**: 77-80.

Ho, C. and S. Khalsa (2012). "A photographic flux mapping mehod for concentrating solar collectors and receivers." Journal of Solar Energy Engineering **134**: 041004-041001 - 041004-041008.

Ingel, G., M. Levy and J. Gordon (1992). "Oil-shale gasification by concentrated sunlight: an open-loop solar chemical heat pipe." Energy **17**(12): 1189-1197.

Johnston, G. (1998). "Focal region measurements of the 20 m2 tiled dish at the Autralian National University." Solar Energy **63**(2): 117-124.
Lee, H., K. Chai, J. Kim, S. Lee, H. Yoon, C. Yu and Y. Kang (2014). "Optical performance evaluation of a solar furnace by measuring the highly concentrated solar flux." Energy **66**: 63-69.
Leibfried, U. and J. Ortjohann (1995). "Convective heat loss from upward and downward-facing cavity solar receivers: measurements and calculations." Journal of Solar Energy Engineering **117**(75-84).
Levy, M., H. Rosin and R. Levitan (1989). "Chemical reactions in a solar furnace by direct solar irradiation of the catalyst." Journal of Solar Energy Engineering **111**: 96-97.
Lewandowski, A., C. Bingham, J. O'Gallagher, R. Winston and D. Sagie (1991). "Performance characterisation of the SERI High-flux solar furnace." Solar Energy Materials **24**: 550-563.
Lim, C. and L. Li (2009). "Flux distribution of solar furnace using non-imaging focusing heliostat." Solar Energy **83**: 1200-1210.
Ma, R. (1993). Wind effects on convective heat loss from a cavity receiver for a parabolic concentrating solar collector. USA, Sandia National Laboratories.
Mojiri, A., C. Stanley and G. Rosengarten (2015). "Close range radiometry for quantifying the spatial distribution of illumination on flat surfaces." Solar Energy **122**: 429-439.
Neumann, A. and U. Groer (1996). "Experimenting with concentrated sunlight using the DLR solar furnace." Solar Energy **58**(4-6): 181-190.
Parretta, A., C. Privato, G. Nenna, A. Antonini and M. Stefancich (2006). "Monitoring of concentrated radiation beam for photovoltaic and thermal solar energy conversion applications." Applied Optics **45**(30): 7885-7896.
Perez-Enciso, R., D. Riveros-Rosas, M. Sanchez, C. Perez-Rabago, C. Arancibia-Bulnes, H. Romero-Paredes and C. Estrada (2014). "Three-dimensional analysis of solar radiation distribution at the focal zone of the solar furnace of IER_UNAM." Energy Procedia **57**: 3031-3040.
Prasad, D., R. guyen and M. Brown (2013). Quick approximation of a camera's spectral response from casual lighting. 2013 IEEE International Conference on Computer Vision Workshops IEEE.
Ries, H. and M. Schubnell (1990). "The optics of a two-stage solar furnace." Solar Energy Materials **21**: 213-217.
Riveros-Rosas, D., J. Herrera-Vasquez, C. Perez-Rabago, C. Arancibia-Bulnes, S. Vasquez-Montiel, M. Sanchez-Gonzalez, F. Granados-Agustin, O. Jaramillo and C. Estrada (2010). "Optical design of a high radiative flux solar furnace for Mexico." Solar Energy **84**: 792-800.
Rodriguez, J., I. Canadas and E. Zarza (2014). "PSA vertical axis solar furnace SF5." Energy Procedia **49**: 1511-1522.
Rohner, N. and A. Neumann (2003). "Measurement of high temperatures in the DLR solar furnace by UV-B detection." Transactions of the ASME **125**: 152-158.
Roldan, M. and R. Monterreal (2014). "Heat flux and temperature predction on a volumetric receiver installed in a solar furnace." Applied Energy **120**: 65-74.
Roldan, M., E. Zarza and J. Casas (2015). "Modelling and testing of a solar-receiver system applied to high-temperature processes." Renewable Energy **76**: 608-618.
Sakurai, T., O. Kamada, K. Shishido and K. Inagaki (1964). "Construction of a large solar furnace." Solar Energy **8**(4): 117-126.
Sammouda, H., C. Royere, A. Belghith and M. Maalej (1999). "Reflected radiance distribution law for a 1000 kW thermal solar furnace system." Renewable Energy **17**: 9-20.
Sarwar, J., G. Georgakis, R. LaChance and N. Ozalp (2014). "Description and characterisation of an adjustable flux solar simulator for solar thermal, thermochemical and photovoltaic applications." Solar Energy **100**: 179-194.

Schubnell, M., J. Keller and A. Imhof (1991). "Flux density distribution in the focal region of a solar concentrator system." Transactions of the ASME **113**: 112-116.
Serth, R. and T. Lestina (2014). Convective and Radiative Heat Transfer. Process Heat Transfer. USA, Academic Press.
Taumoefolau, T., S. Paitoonsurikarn, G. Hughes and K. Lovegrove (2004). "Experimental investigation of natural convection heat loss from a model solar concentrator cavity receiver." Journal of Solar Energy Engineering **126**(801-807).
Taylor, R., M. Yang, A. Bandara, K. Morrison, A. Ashraf and E. Hawkes (2014). Design and analysis of a rooftop solar furnace. Proceedings of the 15th International Heat Transfer Conference Kyoto, Japan.
Trombe, F. and A. Vinh (1973). "Thousand kW solar furnace, built by the National Centre of Scientific Research, in Odeillo (France)." Solar Energy **15**: 57-61.
Ulmer, S., W. Reinalter, P. Heller, E. Lupfert and D. Martinez (2002). "Beam characterisation and improvement with a flux mapping system for dish concentrators." Transactions of the ASME **124**: 182-188.

7. Acknowledgements

The authors thank Herb Hayden and Michael Bading from Southwest Solar LLC for their guidance in calibrating the solar furnace. We also acknowledge Ahmad Mojiri for developing the original MATLAB script for extracting intensity data from the photographic images, and Felipe Crisostomo for his assistance with maintenance and repair of the solar furnace.